

Reservoir characterization using perforation shots: anisotropy, attenuation and uncertainty analysis

Zhishuai Zhang¹,^{ORCID} Jing Du² and Gary M. Mavko¹

¹Department of Geophysics, Stanford University, Stanford, CA 94305, USA. E-mail: zhishuaizhang@gmail.com

²Total E&P Research and Technology, LLC, 1201 Louisiana Street, Suite 1800, Houston, TX 77002, USA

Accepted 2018 October 17. Received 2018 October 12; in original form 2018 March 15

SUMMARY

Anisotropic parameters, when considered in a microseismic processing, are typically inverted using perforation shot data and/or simultaneously inverted with microseismic event locations. Inverting using microseismic data alone usually leads to an underconstrained inverse problem that is highly dependent on prior/initial information. We carefully processed the waveforms from perforation shots, and picked *P*-, *SH*- and *SV*-wave arrival times to mitigate this issue. Because the perforation shot locations are known, the inversion is better constrained by reducing the number of model parameters while increasing the number of observations. We applied both maximum a posteriori estimation and randomized maximum likelihood methods for anisotropic parameter estimation, uncertainty quantification and trade-off analysis. Results verified the stability of the inversion and revealed the uncertainty and trade-offs among model parameter. In addition, attenuation is generally not considered in microseismic modelling and processing. Our study found that hydraulic stimulation may lead strong increases in seismic attenuation to reservoirs. The attenuation can dramatically change waveform characteristics and cause velocity dispersion. Thus, sonic logs, which are acquired at frequencies much higher than seismic data frequency should not be used directly for data processing in hydraulic stimulated zones.

Key words: Fracture and flow; Probability distributions; Tomography; Induced seismicity; Seismic anisotropy; Seismic attenuation.

1 INTRODUCTION

Traditional microseismic monitoring of hydraulic stimulation focuses on characterizing hydraulic fractures with microseismic event locations and source mechanisms (Maxwell 2014; Shapiro 2015; Grechka *et al.* 2017). Attempts have been made to use microseismic data as a source to image the structure of a reservoir and hydraulic fractures (Grechka *et al.* 2017). Perforation shots have been routinely used for velocity model calibration in microseismic processing. Typically, stage-dependent isotropic velocity models are calibrated with perforation shots before each stage to account for heterogeneous and anisotropic effects (Pei *et al.* 2009). However, shales, especially organic-rich shales, are almost always anisotropic (Vernik 2016). A reliable estimation of anisotropic parameters at reservoir *in situ* conditions not only improves microseismic event location accuracy but also is essential for reservoir characterization and providing information for active source surface seismic surveys (Vernik & Nur 1992; Du *et al.* 2013). For instance, anisotropic parameters may be used to infer the content of kerogen in shale (Vernik & Nur 1992). Research on anisotropic earth model characterization has been carried out mainly on simultaneous inversion of microseismic event locations and anisotropic parameters (Grechka *et al.*

2011; Li *et al.* 2013; Yuan & Li 2017). The simultaneous inversion is usually considered as an underconstrained problem and its results are sensitive to prior/initial information such as well logs and presumed anisotropic parameters. To our best knowledge, there has been little effort on trying to construct reliable anisotropic models using only perforation shot data. Building an anisotropic model using only perforation shot data is generally considered to be difficult, if not impossible (Grechka & Heigl 2017; Pei *et al.* 2017).

In this study, we performed check-shot inversion and made efforts to increase the number of observations while reducing the number of model parameters to mitigate this traditionally underconstrained problem. With careful processing, we were able to determine the arrival times of *SV* waves, in addition to the traditionally used *P* and *SH* waves, with high confidence. Using perforation shots instead of microseismic events, source locations, which have trade-offs with velocity parameters (Zhang *et al.* 2017b), do not need to be inverted. These efforts resulted in a well-constrained inverse problem that is insensitive to the prior model.

Another particularly challenging aspect of inverse problems is the quantification of estimation uncertainty and trade-offs among model parameters. While some studies try to quantify microseismic event location uncertainty (Myers *et al.* 2007; Templeton *et al.*

2014; Gesret *et al.* 2015), it is rarely analysed in the earth model building process, which typically dominate the uncertainty of all the subsequent microseismic processing results. In addition, understanding the trade-offs helps when optimizing the parametrization strategy and provides insights into the bias introduced by model simplification. We use both deterministic and stochastic approaches to investigate the uncertainties and trade-offs in velocity model estimation. We developed a Bayesian inversion framework based on our previous work to include anisotropy within the process (Zhang *et al.* 2017b; Zhang *et al.* 2018). To solve for the posterior probability density, we used the maximum a posteriori (MAP) estimation (Tarantola 2005) and the randomized maximum likelihood (RML) method (Oliver *et al.* 1996). Results show the stability of the inversion and help us to understand the uncertainty and trade-offs between model parameters.

The importance of estimating attenuation parameters lies in several aspects. First, seismic attenuation acts as a low-pass filter that modifies the frequency content of seismic waves. Thus, it is a requirement for understanding and making any use of the full waveform information. Secondly, the Q value can be a parameter to understand the *in situ* conditions of the target formation. According to Ou & Prasad (2016), the attenuation might be a better indication of pressure change than the P -wave velocity. Klimentos (1995) showed that Q values may be used to distinguish gas and condensate from oil and water. Tan *et al.* (2014) showed severe S -wave attenuation caused by water-filled hydraulic fractures. Thirdly, a reliable estimation of earthquake source parameters depends on the availability of seismic attenuation information. The seismic amplitude received by a geophone is a coupled effect of source magnitude, radiation pattern, seismic wave geometric spreading and path attenuation. The estimation of attenuation parameters helps to constrain source magnitude and source mechanism. Finally, attenuation causes velocity dispersion (Toll 1956). Due to the dispersion, the sonic logs acquired at high frequency may not be a good representation of the velocity at the seismic or microseismic frequency. An estimation of attenuation gives a heads up about this possible discrepancy. There are only a limited number of studies to investigate the Q value changes due to fluid injection. Zhu *et al.* (2017) studied the spatial and temporal attenuation changes induced by the variation of CO_2 saturation when maintaining the pore pressure. Vera Rodriguez & Stanchits (2017) investigated the spatial and temporal variations of attenuation during hydraulic fracturing with a laboratory experiment. The determination of Q values can be from surface reflection seismology (Shen *et al.* 2018a,b), crosswell (Quan & Harris 1997), or vertical seismic profile (VSP) data (Tonn 1991). In microseismic processing, limited attempts have been made to estimate Q values (Eisner *et al.* 2013; Wcisło & Eisner 2016; Li *et al.* 2017; Wandycz *et al.* 2017; Wcisło & Eisner 2017). However, in practical microseismic processing, the seismic attenuation is typically not considered or the Q value is assumed to be temporal invariant. Here, we use the spectral-ratio method to estimate Q values using perforation shots and microseismic data (Tonn 1991). The estimated stage-dependent attenuation reveals the possible effect introduced by hydraulic stimulation. It also suggests that downhole seismic surveys can be a suitable tool to monitor this process with attenuation parameter estimation.

The paper is organized as follows. In Section 2, we present the Bayesian framework for the anisotropic problem and its MAP and RML solutions. We also show the application of the spectral-ratio method to the microseismic data set. Then, we review the field setup of the survey at the Vaca Muerta formation. After that, we show the results of anisotropic parameter estimation and analysis

of uncertainty and trade-offs. Following this anisotropy section, we discuss the Q values obtained and their implication and potential applications. Finally, we conclude with discussion on the limitation of this work and the possible impact of our findings.

2 METHODOLOGY

2.1 Thomsen parameter estimation with Bayesian inference

We have developed a Bayesian inference framework to simultaneously invert for microseismic event locations and velocity model. The method has been successfully applied to a shallow borehole survey in the Newberry Enhanced Geothermal System (Zhang *et al.* 2017b) and a downhole survey in the Vaca Muerta Formation (Zhang *et al.* 2018). In this section, we generalized this method to anisotropic studies with a vertical transverse isotropic (VTI) model.

We assume that the perforation shot and geophone locations can be obtained from the deviation survey with sufficient accuracy. The earth model consists of anisotropic layers with boundaries predetermined based on sonic and gamma-ray logs. The model parameters to be estimated include those characterizing the properties of each layer and the origin time of each perforation. For a system with N perforations and M layers, the model parameter set \mathbf{m} consists of $N + 5M$ elements:

$$\mathbf{m} = [t_1, t_2, \dots, t_s, \dots, t_N; \mathbf{V}_1, \mathbf{V}_2, \dots, \mathbf{V}_l, \dots, \mathbf{V}_M]^T, \quad (1)$$

where t_s is the origin time of the s th perforation shot. $\mathbf{V}_l = [Vp(0)_l, Vs(0)_l, \varepsilon_l, \gamma_l, \delta_l]$ are the Thomsen parameters of the l th layer (Thomsen 1986). For VTI material, $Vp(0)$ and $Vs(0)$ are the vertical propagating P - and S -wave velocities, respectively. In the case of weak anisotropy, ε can be seen as the fractional difference between vertically and horizontally propagating P -wave velocities. γ can be considered as the fractional difference between vertically and horizontally propagating SH -wave velocities. δ controls the nearly vertical propagating P -wave velocity. \mathbf{T} represents the transpose of a matrix.

The observation vector \mathbf{d}_{obs} includes all available P -, SH - and SV -wave arrival times that can be picked with adequate confidence. The forward operator $\mathbf{g}(\cdot)$ is to predict the observable parameters using a given set of model parameters \mathbf{m} . We use a 3-D anisotropic eikonal solver developed by Belayouni *et al.* (2016) for forward modelling. Specifically, it calculates the arrival times of each phase at all geophone locations by solving an eikonal equation in VTI medium. Detailed information about the forward modelling method was given by Noble *et al.* (2014) and Belayouni *et al.* (2016).

According to inverse theory (Tarantola 2005; Zhang *et al.* 2017b), under the Gaussian assumption the posterior probability density of model parameters is given by

$$\sigma_M(\mathbf{m}) = c \exp \left\{ -\frac{1}{2} [\mathbf{g}(\mathbf{m}) - \mathbf{d}_{\text{obs}}]^T \mathbf{C}_D^{-1} [\mathbf{g}(\mathbf{m}) - \mathbf{d}_{\text{obs}}] - \frac{1}{2} (\mathbf{m} - \mathbf{m}_{\text{prior}})^T \mathbf{C}_m^{-1} (\mathbf{m} - \mathbf{m}_{\text{prior}}) \right\}, \quad (2)$$

where $\mathbf{m}_{\text{prior}}$ is the vector of prior mean values of the model parameters. The covariance matrix \mathbf{C}_D is the summation of the measurement uncertainty part \mathbf{C}_d and the parametrization uncertainty part \mathbf{C}_T . \mathbf{C}_m is the covariance matrix of the prior information. c is a normalization constant. A detailed discussion of eq. (2) was presented by Tarantola (2005) and Zhang *et al.* (2017b).

2.2 Maximum a posteriori estimation

An efficient way to solve the inverse problem formulated by eq. (2) is to estimate the MAP point \mathbf{m}_{MAP} , along with its covariance matrix $\mathbf{C}_{\text{m,MAP}}$ to characterize the posterior probability density of model parameters (Zhang *et al.* 2017b):

$$\mathbf{m}_{\text{MAP}} = \arg \max_{\mathbf{m}} \sigma_M(\mathbf{m}) \quad (3)$$

and

$$\mathbf{C}_{\text{m,MAP}} = \mathbf{C}_{\text{m}} - \mathbf{C}_{\text{m}} \mathbf{G}_{\text{MAP}}^T (\mathbf{G}_{\text{MAP}} \mathbf{C}_{\text{m}} \mathbf{G}_{\text{MAP}}^T + \mathbf{C}_{\text{D}})^{-1} \mathbf{G}_{\text{MAP}} \mathbf{C}_{\text{m}}, \quad (4)$$

where \mathbf{G}_{MAP} is the sensitivity matrix with elements $G_{ij} = \frac{\partial g_i}{\partial m_j}$ at the MAP point \mathbf{m}_{MAP} . g_i is the i th element of $\mathbf{g}(\cdot)$ and m_j is the j th element of \mathbf{m} .

A more intuitive but less computationally efficient equivalent form of eq. (4) is

$$\mathbf{C}_{\text{m,MAP}} = (\mathbf{G}_{\text{MAP}}^T \mathbf{C}_{\text{D}}^{-1} \mathbf{G}_{\text{MAP}} + \mathbf{C}_{\text{M}}^{-1})^{-1}, \quad (5)$$

where $\mathbf{H} = \mathbf{G}_{\text{MAP}}^T \mathbf{C}_{\text{D}}^{-1} \mathbf{G}_{\text{MAP}}$ is known as the Gauss–Newton approximation of the data misfit Hessian (Pratt *et al.* 1998; Zhu *et al.* 2016). It is apparent from this expression that the posterior covariance matrix has the advantage over the inverse Hessian in this case by taking the prior information into consideration.

Even though the MAP estimation is exact only when all the information is of Gaussian type and the operator $\mathbf{g}(\cdot)$ is linear, which are usually not the case, it is efficient in terms of computation and is normally a reasonable approximation to the posterior probability density. The maximization of eq. (3) can be achieved with various methods including steepest descent (Tarantola 2005; Aster *et al.* 2011), Newton’s method (Aster *et al.* 2011), Gauss–Newton method (Zhang *et al.* 2014; Zhang *et al.* 2017b,a), conjugate gradient (Aster *et al.* 2011) and truncated-Newton methods (Hessian-free optimization, Nash 2000; Pan *et al.* 2017). In this study, the \mathbf{m}_{MAP} is achieved with a Gauss–Newton method (Zhang *et al.* 2014; Zhang *et al.* 2017a,b), which is a modification to Newton’s method to iteratively minimize a sum of squared function values without a computation of Hessian.

2.3 Randomized maximum likelihood method

The MAP estimation described above requires a Gaussian distribution for all the information and the linearity of the forward operator, which is an approximation to real problems. A proper way to tackle non-Gaussian and non-linear inverse problem is to use the Markov chain Monte Carlo (MCMC) method. However, the MCMC can be computationally expensive for problems with large model dimensions. Here, we use the RML method to approximate the McMC method (Oliver *et al.* 1996). The motivation of using the RML method is twofold: first, it allows us to test the sensitivity of the inversion results to the prior velocity model, which is important to make sure that the inverse problem is well constrained; secondly, it provides an adequate approximation to the McMC method and does not require the Gaussian and linear assumptions as is required in the MAP estimation (Oliver *et al.* 1996). The RML method conditions an unconditional realization of model parameters on the observed arrival times by minimizing the objective function:

$$J(\mathbf{m}) = [\mathbf{g}(\mathbf{m}) - \mathbf{d}_u]^T \mathbf{C}_{\text{D}}^{-1} [\mathbf{g}(\mathbf{m}) - \mathbf{d}_u] + (\mathbf{m} - \mathbf{m}_u)^T \mathbf{C}_{\text{m}}^{-1} (\mathbf{m} - \mathbf{m}_u), \quad (6)$$

where \mathbf{d}_u is a set of perturbed observations obtained by adding zero-mean Gaussian random noises with covariance \mathbf{C}_{D} to arrival

time pickings. \mathbf{m}_u represents an unconditional realization of the model parameters. It can be generated by drawing a random sample from the distribution described by $\mathbf{m}_{\text{prior}}$ as the mean and \mathbf{C}_{m} as the covariance. To generate N conditional realizations of the earth model, eq. (6) needs to be minimized N times with a different unconditional model parameter \mathbf{m}_u and perturbed observation \mathbf{d}_u each time.

2.4 Spectral-ratio method for Q value estimation

The spectral-ratio method in a VSP survey estimates Q values using the fact that high-frequency waves have greater attenuation than low-frequency waves along the same travel path (Tonn 1991). It has the advantage of not being affected by the radiation pattern of the source, which is generally unknown and usually varies among individual perforations. The microseismic monitoring project in this study involves stimulation stages in a horizontal well and a geophone array in a nearby vertical well (Fig. 1). This makes the survey resemble the configuration of a walkaway VSP. We are able to estimate the Q values using perforation shots as well as microseismic event signals.

Consider the wave paths for a specific phase (P , SH or SV) from the same source to two different geophones, which will be referred as a geophone pair in the following discussion. The difference in the two paths will cause a difference in spectrum due to attenuation, reflection and geometrical spreading. The dependence of these two waveform amplitudes A_1 and A_2 on the Q value for this specific phase are given by

$$A_1 = G_1 \cdot R_1 \cdot A_0 \exp\left(-\frac{\pi f x_1}{V Q}\right) \quad (7)$$

and

$$A_2 = G_2 \cdot R_2 \cdot A_0 \exp\left(-\frac{\pi f x_2}{V Q}\right), \quad (8)$$

where G_1 and G_2 are the geometrical spreading factors, R_1 and R_2 are the reflection coefficients, A_0 is the original amplitude, x_1 and x_2 are the path lengths travelled by the two seismic rays and f and V are wave frequency and velocity, respectively.

The ratio between eqs (8) and (7) is

$$\begin{aligned} \frac{A_2}{A_1} &= \frac{G_2}{G_1} \cdot \frac{R_2}{R_1} \cdot \exp\left(-\frac{\pi f x_2 - x_1}{Q V}\right) \\ &= \frac{G_2}{G_1} \cdot \frac{R_2}{R_1} \cdot \exp\left(-\frac{\pi f}{Q} \Delta t\right), \end{aligned} \quad (9)$$

where $\Delta t = \frac{x_2 - x_1}{V} = t_2 - t_1$ and t_1 and t_2 are the traveltimes from the source to the two geophones, respectively.

Taking the natural log of eq. (9) and dividing each side by Δt , we get

$$\frac{1}{\Delta t} \ln \frac{A_2}{A_1} = -\frac{\pi}{Q} f + \frac{1}{\Delta t} \ln \frac{G_2 R_2}{G_1 R_1} = -\frac{\pi}{Q} f + C, \quad (10)$$

where $C = \frac{1}{\Delta t} \ln \frac{G_2 R_2}{G_1 R_1}$ is a constant for each geophone pair. The relationship between $\frac{1}{\Delta t} \ln \frac{A_2}{A_1}$ and f in eq. (10) is linear and the slope is $-\frac{\pi}{Q}$. Seismic waves from the same source to various geophone pairs give a set of parallel lines with the same slope $-\frac{\pi}{Q}$. We can compile these lines to stabilize the estimation of the slope. In this study, we make the assumption that the Q values are independent of frequency and homogeneous over the studied area.

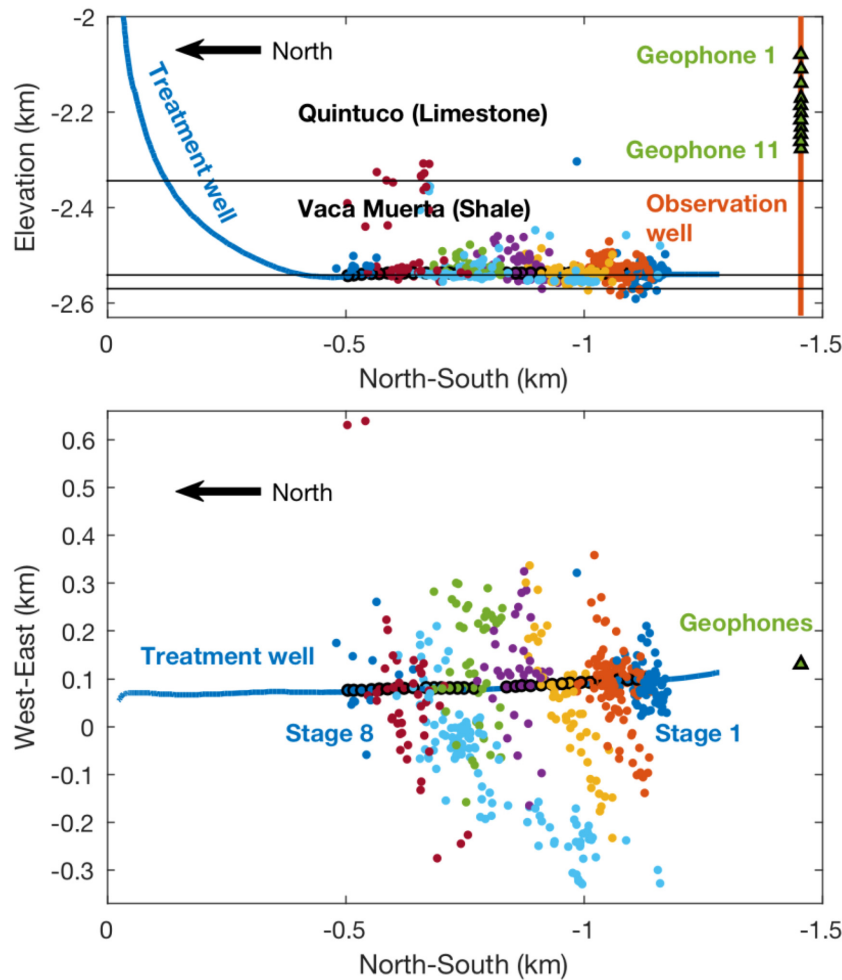


Figure 1. Microseismic survey project setup (side and map views). A total of eight stimulation stages were conducted. The associated microseismic events processed by a contractor are colour coded according to their stages. The stimulation was monitored with a 22-tool, 11-level double-stacked geophone array in an adjacent vertical observation well.

3 HYDRAULIC FRACTURING PROJECT OVERVIEW

The hydraulic fracturing stimulation was conducted with a horizontal well in the Vaca Muerta Formation at Neuquén, Argentina. The Vaca Muerta Formation is associated with the Late Jurassic mixed shale lithology with calcareous and silicoclastic rocks. It is developed along the northwestern part of the Neuquén Basin (Willis *et al.* 2014). The Vaca Muerta Formation consists of three members. The lower Vaca Muerta is organic-rich shale. The middle Vaca Muerta shows less lamination and lower TOC content. The upper Vaca Muerta is also more organic rich and laminated like the lower member (García *et al.* 2013). The overlying Quintuco formation is primarily a limestone reservoir with dolomite and anhydrite. The underlying Tordillo is a clastic reservoir deposited through aeolian and lacustrine mechanisms (Willis *et al.* 2014). The Vaca Muerta has been targeted as a prospective tight gas and oil play. It is similar to Eagle Ford, where there are oil, wet gas and dry gas windows when moving from east to west. The area studied in this work lies in the wet gas window of the play.

The side and map views of the project are shown in Fig. 1. The stimulation well is perpendicular to the expected fracture azimuth in the Vaca Muerta. It is completed as a cemented lateral using a plug and perf. A total of eight hydraulic fracturing treatment stages

Table 1. Number of triggered microseismic events within each stimulation stage.

Stage	Number of events
1	66
2	123
3	53
4	37
5	44
6	116
7	42
8	11

were performed. Each stimulation stage follows four perforation shots. The stimulation process was monitored with an array of 11 geophones in a nearby vertical well. The geophones and perforation shots are almost in the same vertical plane. The vertical spacing is approximately 30.5 m for the top four geophones and is approximately 15.2 m for the bottom eight geophones. The sampling interval of the recording is 0.375 ms.

All the 32 perforation shots were recorded, and a total of 492 microseismic events were triggered and processed by a contractor using standard industrial practice (Fig. 1). The numbers of microseismic events triggered in each stage are shown in Table 1. In

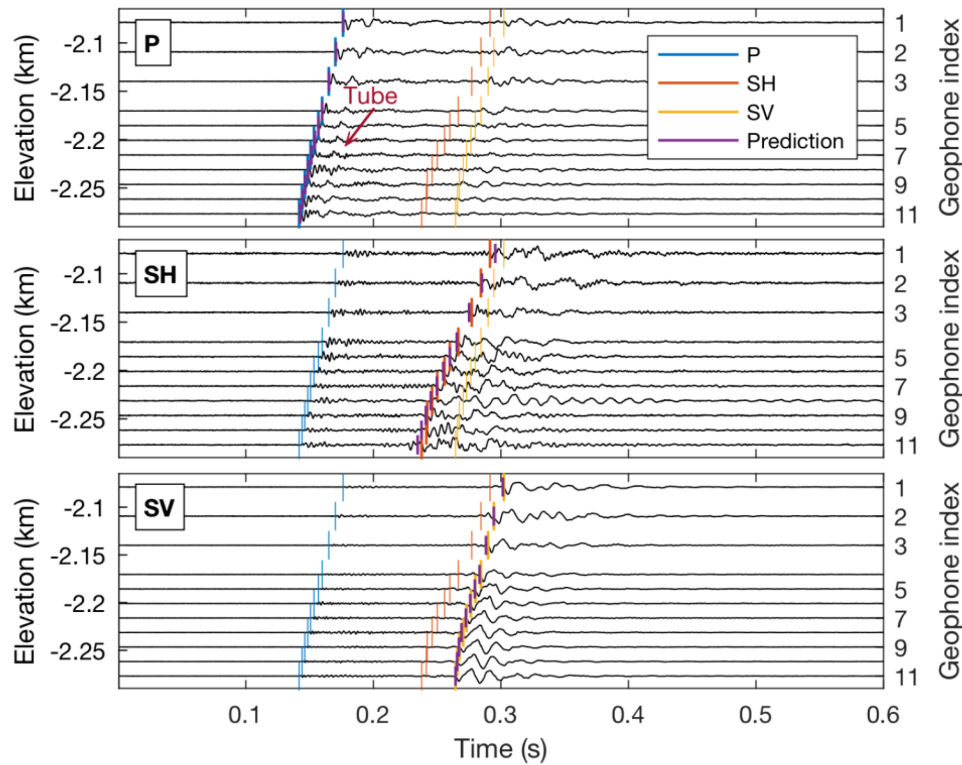


Figure 2. Sample waveforms from the first perforation in stimulation Stage 2. Waveforms are rotated to separate P -, SH - and SV -wave components. The blue, orange and yellow lines are manually picked arrival times and the purple arrival times are predicted arrival times using the MAP estimated model. Thinner lines represent pickings in other components for reference purposes. The phase annotated by the red arrow in the P -wave panel is tube wave as discussed in our previous study (Bergery *et al.* 2017).

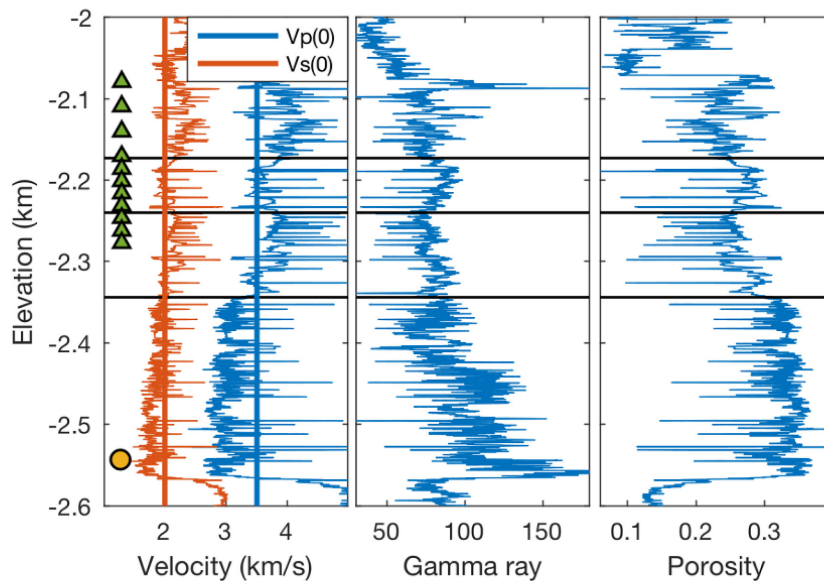


Figure 3. A four-layer homogeneous isotropic prior/initial velocity model was used in the inversion. The layer interfaces (black lines) are positioned based on well logs and sensitivity to arrival times. The thick bottom layer is due to lack of sensitivity to arrival times.

the contractor's processing, an initial layered isotropic elastic earth model was built based on sonic logs from the observation well. Then, it was calibrated with perforation shots and early microseismic events for each stimulation stage. P - and S -wave arrival times are picked manually. Microseismic events were located by minimizing the misfit between the picked and predicted arrival times of the eikonal equation solver.

4 ANISOTROPY

Sample waveforms from the first perforation in stimulation Stage 2 are shown in Fig. 2. They are rotated based on P -wave polarization direction to separate P -, SH - and SV -wave components. The phase annotated by the red arrow in the P -wave panel is a tube wave as discussed in our previous study (Bergery *et al.* 2017). We can

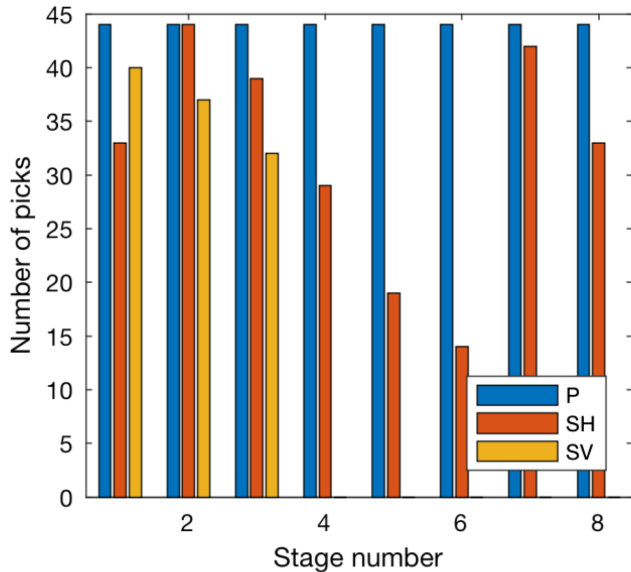


Figure 4. Number of arrival time picks in each stage used for inversion. *SV*-wave arrival times from the first three stimulation stages are used for inversion and those from the last five stages are left for prediction uncertainty quantification.

see clear shear wave splitting as indicated by the manually picked *SH*- and *SV*-wave arrival times. This is an effect of anisotropy and indicates the necessity of taking it into consideration.

4.1 Prior/initial model

We divided the studied area into four horizontal layers based on well logs and sensitivities to arrival times as shown in Fig. 3. The reason to leave the bottom layer relatively thick is the lack of sensitivity of arrival times to wave velocities at this layer. We refer to the top layer as the first layer and the bottom layer as the fourth layer. The initial model is a homogeneous isotropic one. The prior mean of vertically propagating velocities $V_p(0)$ and $V_s(0)$ are 3.5 and 2.0 km s⁻¹, respectively. Their standard deviation (SD) is 0.5 km s⁻¹. The prior mean values of Thomsen parameters ϵ , δ and γ are all zero with an SD of 0.5. The initial origin time of each perforation shot is 0.2 s before the earliest picking with an SD of 3 s. The initial model used in the MAP estimation is taken as the same as the prior model. The unconstrained realizations used in the RML method are drawn from their corresponding Gaussian distributions.

4.2 Observations

The observations are manually picked arrival times of *P*, *SH* and *SV* waves. We picked *P*- and *SH*-wave arrival times for all perforation shots whenever we were able to do so confidently. The *SV*-wave arrival times for the 12 perforation shots in the first three stimulation stages were also picked. The *SV*-wave arrival times for Stages 4–8 were not used for two reasons: (1) the *SV*-wave arrival times in the later stages can be used to quantify the prediction error of the calibrated model; (2) it is difficult to pick the *SV*-wave arrival times in these stages due to contamination of an earlier phase with similar polarization direction with the *SV* waves, which may be *P*–*SV* converted waves. The picked arrival times on the first perforation in Stage 2 are shown in Fig. 2. The statistics of the number of picked arrival times by stage are shown in Fig. 4. We used an SD of 1.0 ms

for *P*-wave arrival time uncertainty and 2.0 ms for *SH*- and *SV*-wave uncertainty.

4.3 RESULTS

4.3.1 MAP estimation

The MAP estimated model is shown in Fig. 5 along with the sonic and gamma-ray logs. The estimated vertically propagating *P*- and *S*-wave velocities match the sonic log velocities well for the top three layers. However, those for the bottom layer are significantly smaller than the sonic velocities. This discrepancy might be a result of velocity dispersion and will be discussed in Section 5. The inverted ϵ , δ and γ values are almost all positive. We found that the velocities tend to be slower in the second and the bottom layers where the gamma-ray value (clay content) is high. This is consistent with our knowledge of the effect of clay content on seismic wave velocities (Han *et al.* 1986; Mavko *et al.* 2009). The anisotropic parameters are also higher in these two layers, which mean increased anisotropy associated with increased clay content. The predicted arrival times using the inverted anisotropic model are shown by the purple picks in Fig. 2 (Stage 2, Perforation 1) and Fig. 6 (Stage 6, Perforation 2). Only *SV*-wave arrival times from Stages 1 to 3 are used for inversion, so those in later stages can be used to validate the inverted model. The predicted *SV*-wave arrival times in Fig. 6 match well with the waveforms. Also note the phase indicated by the red question mark in the *SV*-wave component panel, which might be *P*–*SV* converted waves. This phase can be misinterpreted as the direct *SV* wave without the prediction from the inverted model. The statistics of the arrival time residuals of the anisotropic earth model estimation are shown in Fig. 7. For each phase, the arrival time residuals are nearly evenly distributed among stages. The inverted anisotropic velocity model was also used to locate microseismic events. Only *P*- and *SH*-wave arrival times were used in the microseismic location estimation. With the estimated locations, predictions of *SV*-wave arrival times can be made and are shown in Fig. 8. Similar with Fig. 6, the predicted *SV*-wave arrival times match well with the waveforms although the *SV*-wave arrival times are not used for event location.

The estimated V_p and V_s values under the assumption of isotropic earth model are also shown in Fig. 5. The observations used in the isotropic case are the *P*- and *S*-wave arrival times (*SH*- instead of *SV*-wave arrival times from the data are used). Comparing the V_p and V_s values in the isotropic case to the $V_p(0)$ and $V_s(0)$ values estimated in the anisotropic case, even though the V_p and V_s values at the bottom layer in the isotropic case match the sonic logs better, the V_p values are significantly slower than the sonic logs at the top three layers. The difference between the isotropic and anisotropic estimation results is due to the false isotropic earth model assumption in the former case. This point will be further illustrated in Section 4.3.3 to be attributed to the effect of forcing ϵ , δ and γ to be zero under the isotropic assumption.

4.3.2 RML method

We generated 60 realizations from the posterior probability density function with the RML method. Then, the histogram of each variable was fitted with a kernel smoother and the result is shown in Fig. 9. The overlain orange lines represent the MAP estimation results for comparison purposes. In general, the RML result matches

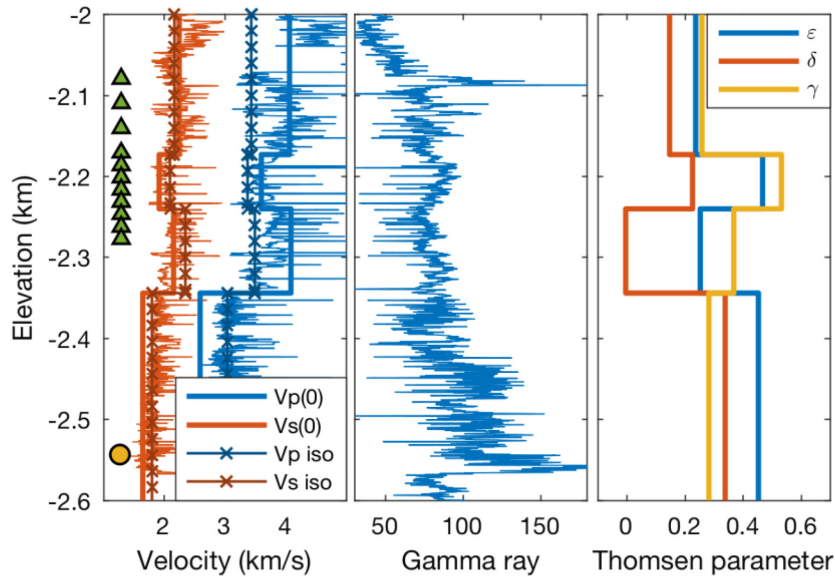


Figure 5. MAP estimated velocity model with well logs as the background. The estimated $V_p(0)$ and $V_s(0)$ values match the sonic log well at the top three layers. The discrepancy at the bottom layer will be discussed in the Attenuation section. The estimated V_p and V_s values under the assumption of isotropic earth model are also shown. The studied area is moderate anisotropy according to the inversion. Comparing to the gamma-ray log, the velocities of vertically propagating waves tend to decrease and anisotropy tends to increase at the second and the bottom layers where the clay content (Gamma ray) is high.

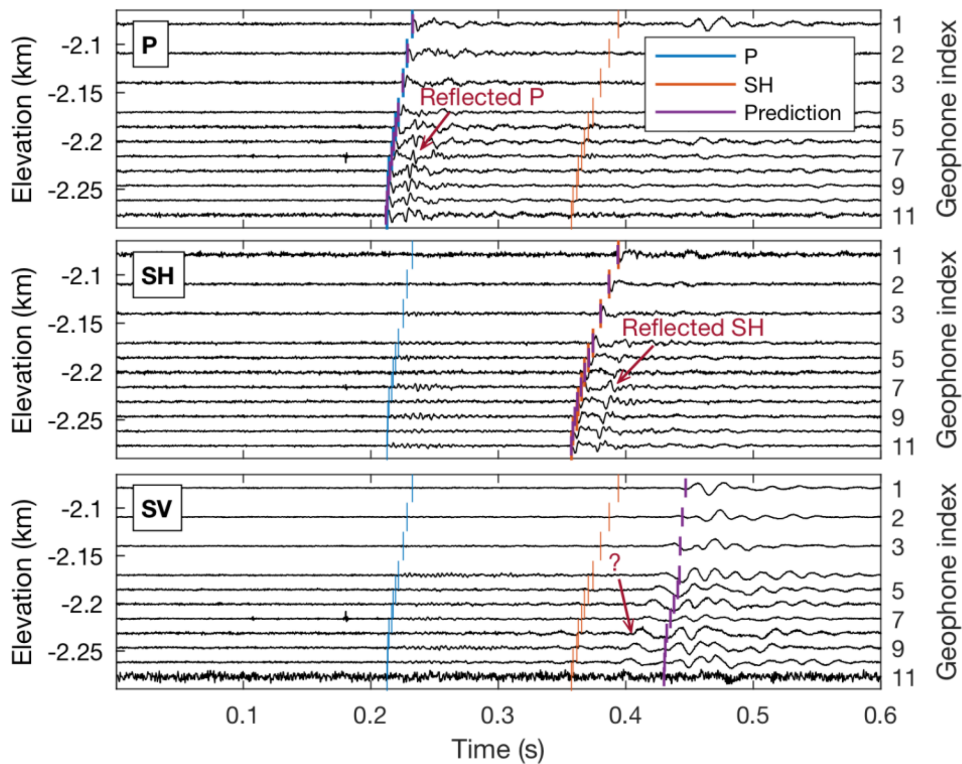


Figure 6. Waveforms from the second perforation in Stage 6 stimulation. They are rotated to separate P -, SH - and SV -wave components. Even though SV -wave arrival times are not used in the velocity model estimation, the predictions given by the estimated model match the waveforms well. The unknown phase annotated by the question mark may be misidentified as SV wave otherwise. The phase annotated by the red arrow in the P - and SH -wave panel are reflected waves from an underlying high velocity layer (do not be confused with the tube wave in Fig. 2).

the MAP estimation well. From the RML result, we can see increased velocity estimation uncertainty with depth. The uncertainty for the δ value of the third layer is also large, and this corresponds to the only near-zero anisotropic parameter. The scatter plots of

various parameter pairs from the RML estimation are shown by the green dots in Fig. 10. Only $V_p(0)$ of the four layers and the other four anisotropic parameters at the fourth layer are shown for simplicity. The overlain MAP-estimated 99 per cent confidence intervals given

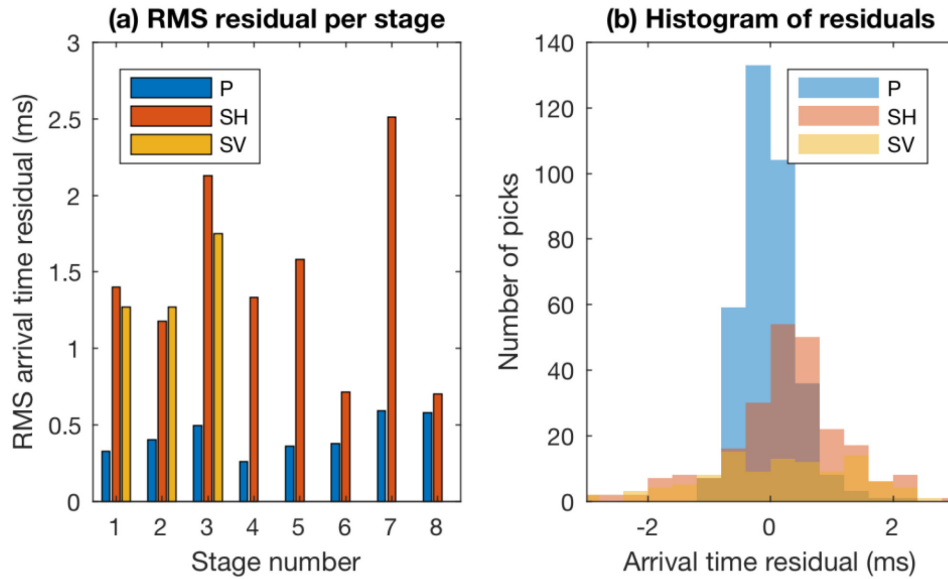


Figure 7. a) RMS of the arrival time residuals by stage and (b) histogram of arrival time residuals by phase.

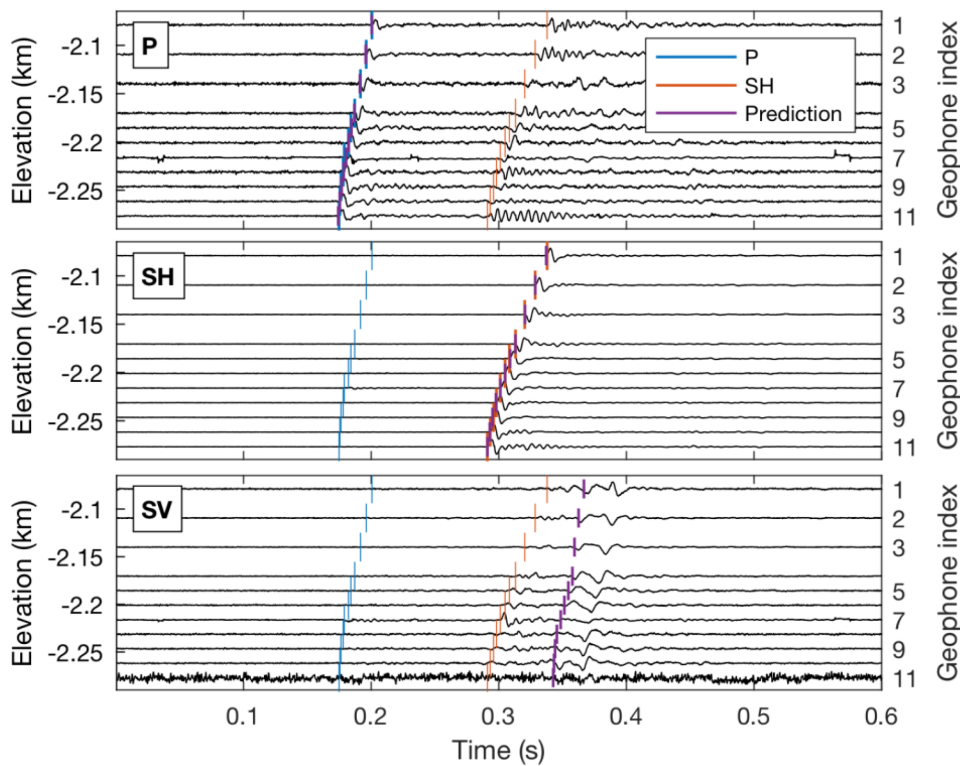


Figure 8. Waveforms from a typical microseismic event. The *SH*-wave components have higher signal-to-noise ratio (S/N) than those from the perforation shot due to the shear motion dominant nature of a typical microseismic event. Even though *SV*-wave arrival times are not used in microseismic event location, the predictions given by the estimated event location match the waveforms well.

by eq. (4) are represented by the black ellipses. The correlation coefficient between each parameter pair is represented by the background colour. The MAP estimation was able to match the general trend of the RML result. However, the RML estimated uncertainties are significantly larger and deviate from Gaussian distribution due to the non-linearity of the problem.

4.3.3 Trade-offs between model parameters

In simultaneous inversion of multiple parameters such as the case in our problem, the trade-offs between model parameters may result in unreliable estimations. MAP and RML estimation provide insight into these trade-offs. In addition, the quantification of trade-offs between model parameters improve our understanding of the

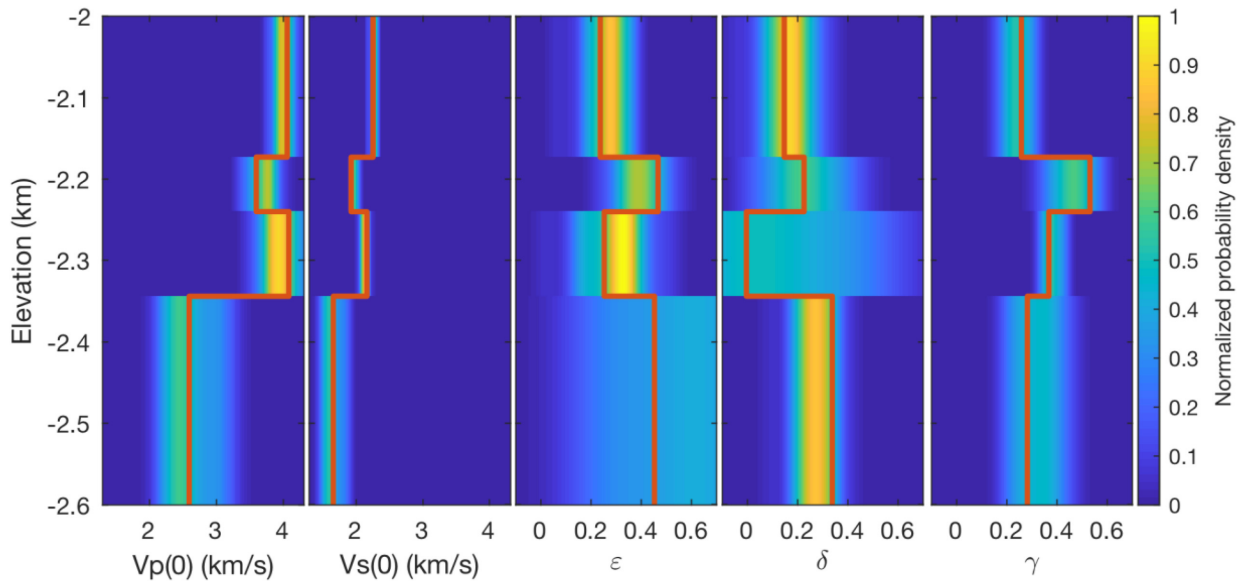


Figure 9. RML estimated probability density overlain by the MAP estimated result (orange lines). The estimation uncertainty at the bottom layer is large due to the lack of sensitivity to arrival times.

bias introduced by making unrealistic assumptions such as isotropic earth model. Here, we give a discussion about the trade-offs of a couple of parameter pairs for illustration purposes.

According to the correlation coefficients shown in Fig. 10, one of the parameter pairs with the strongest trade-offs is $V_p(0)$ and $V_s(0)$ (middle square with white frames in Fig. 10). This is a result of the unknown origin times of perforation shots and the well-known P - and SH -wave arrival time differences. The correlations among anisotropic parameters in the fourth layer are usually strong (rectangles with white, yellow, black, and blue frames in Fig. 10). However, the correlation coefficients between $V_p(0)$ values at the top three layers and that at the bottom layer is not as significant (rectangles with green frames in Fig. 10). This indicates the strongest trade-offs occur within different parameters in the same layer instead of among the same parameter of different layers.

The $V_p(0)$ and $V_s(0)$ values at the fourth layer have relatively strong negative correlation with the three Thomsen parameters ϵ , δ and γ at the fourth layer. These negative correlations can be attributed to the summation nature between the vertically propagating velocities and Thomsen parameters as shown by eqs (10v) and (16) in Thomsen's (1986) paper on weak elastic anisotropy. The overestimated value of $V_p(0)$ and $V_s(0)$ at the fourth layer for the isotropic case (Fig. 5) can be understood as the following: assuming an isotropic earth model means constraining the Thomsen parameters to be zero. By forcing the values of ϵ , δ and γ to be smaller than their actual values, the estimated values of $V_p(0)$ and $V_s(0)$ are larger than their actual values according to their negative correlations with the three Thomsen parameters (rectangles with yellow frames in Fig. 10). The parameter δ has no correlation with γ (squares with blue frames in Fig. 10) since it is unrelated to the velocity of SH waves.

5 ATTENUATION

A zoom-in view of the P -wave component from Fig. 2 is shown in Fig. 11(a). We can see clear change in frequency content from the top geophones to the bottom ones. We attribute this change to

attenuation along the paths of the seismic waves. With the spectral-ratio method, we may estimate the Q values along the path. Due to limitation in signal-to-noise ratio (S/N) and ray path coverage, we assumed isotropic and homogeneous Q value within the whole model. This represents the average Q values along the seismic paths. A Tukey window was applied to extract the P wave from the whole waveform. An example spectral-ratio fit is shown in Fig. 11(c). The Q value can be estimated using the slope of the least-squares fitted straight line. The uncertainty of the Q value can also be obtained from the uncertainty of the fitted slope. The estimated Q_p value from this spectrum is 11.5, which means significant attenuation within the area.

5.1 Intrinsic versus scattering Q

To investigate the origin of the attenuation, we first tried to distinguish the intrinsic Q from the stratigraphic scattering Q . Under the assumption that the vertical heterogeneity is more significant than the lateral heterogeneity, we constructed a 1-D layered earth model from the sonic logs. We carried out 2-D isotropic synthetic waveform modelling with the wavenumber integration method using Herrmann's (2013) code. To approximate the effect of stratigraphic scattering Q , we divided the P -wave sonic log into 154 layers as shown by the orange line in Fig. 12. The V_s values were approximated with an assumed V_p/V_s of 1.73. The density was estimated with the Gardner's relation (Gardner *et al.* 1974). No intrinsic attenuation was used in the modelling. The P -wave portion of the synthetic waveform is shown in Fig. 11(b), and its corresponding spectral-ratio fit is shown in Fig. 11(d). Fig. 13 shows the whole synthetic waveform. From Fig. 11(b), we can see that the elastic model predicts no clear change in frequency content for difference geophones. This is also shown by the nearly flat fitted line in Fig. 11(d). This suggests that the stratigraphic scattering attenuation does not contribute a significant portion to the overall attenuation. Thus, we conclude that the dispersion is mainly a result of intrinsic attenuation.

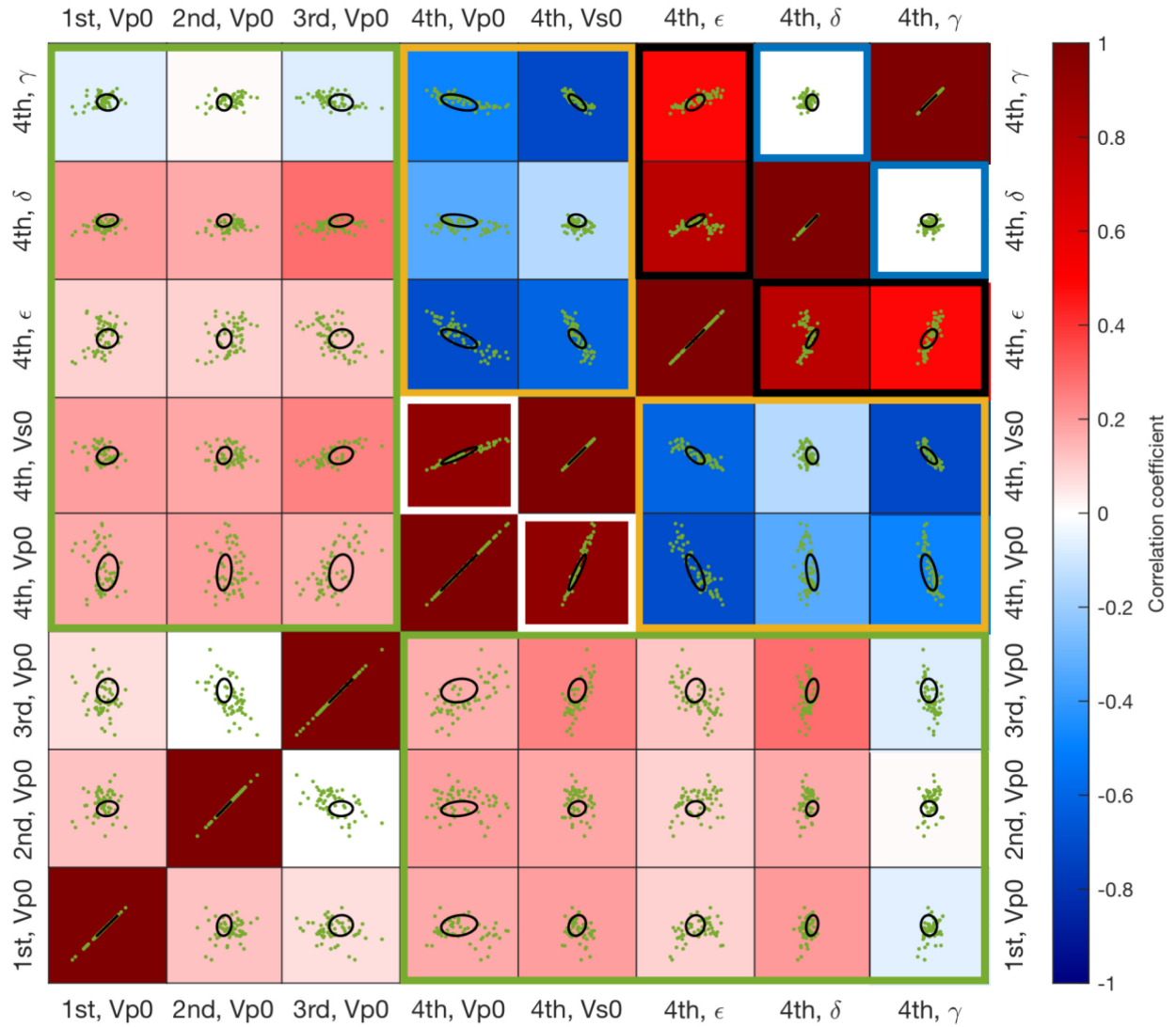


Figure 10. Green dots represent the scatter plots of various parameter pairs from the RML estimation. Only $V_p(0)$ of the four layers and the other four anisotropic parameters at the fourth layer are shown for simplicity. The overlain black ellipses are the MAP-estimated 99 per cent confidence intervals. The axis ranges for $V_p(0)$ and $V_s(0)$ are $V_p(0)_{\text{MAP}} \pm 0.8$ and $V_s(0)_{\text{MAP}} \pm 0.8$ km, respectively. The axis ranges for ϵ , δ and γ are $\epsilon_{\text{MAP}} \pm 0.8$, $\delta_{\text{MAP}} \pm 0.8$ and $\gamma_{\text{MAP}} \pm 0.8$, respectively. The correlation coefficient between each parameter pair is represented by the background colour. While the MAP estimation significantly underestimate the uncertainty of these values due to linear assumption, it predicts the trend and correlation correctly.

5.2 Q_p values from perforation shots

We first calculate the Q_p values using perforation shot signals. Due to the explosion-dominated nature of a perforation shot's source mechanism, the SH -wave component suffers from low S/N. Thus, Q_s values were not analysed. To achieve a reliable estimation result, we used only perforation shots that can give a reasonable linear relationship between spectral ratio and frequency. Based on this criterion, 11 out of the 32 perforation shots were automatically selected. All the perforation shots from Stages 5 to 8 are automatically discarded due to low S/N. The Q_p values estimated from these perforations are shown by the histogram in Fig. 14(a). This histogram shows that the majority of these events give Q_p values between 10 and 15, while there are three outliers whose Q_p values lie around 25 or 30 that will be discussed next. Fig. 15 shows the estimated Q_p values with their perforation shot locations. The error bars stand for the 95 per cent confidence intervals of these values. It is apparent

that the perforation shots with high Q_p values (the three outliers in Fig. 14a) are all from Stage 1, which is the only stage where no hydraulic fracturing stimulation was conducted before the perforation. Thus, we consider these Q_p values represent the original attenuation of the unstimulated reservoir. After Stage 1, the ray paths of the perforation shots will somewhat overlap with the zones affected by previous stimulations (Fig. 16). The significant decrease in the Q_p values estimated from later stages perforation shots may be related to the stimulation of the formation. The hydraulic stimulation introduces changes to the formation from several aspects: creation of new fractures or the stimulation of pre-existing fractures; change in fluid saturation and change in *in situ* stress states. According to Amalokwu *et al.* (2014), P -wave attenuation is not significantly increased by the presence of fractures as long as the fracture aperture is much less than the wavelength. Thus, the increased P -wave attenuation should be attributed mainly to changes in water saturation and stress states.

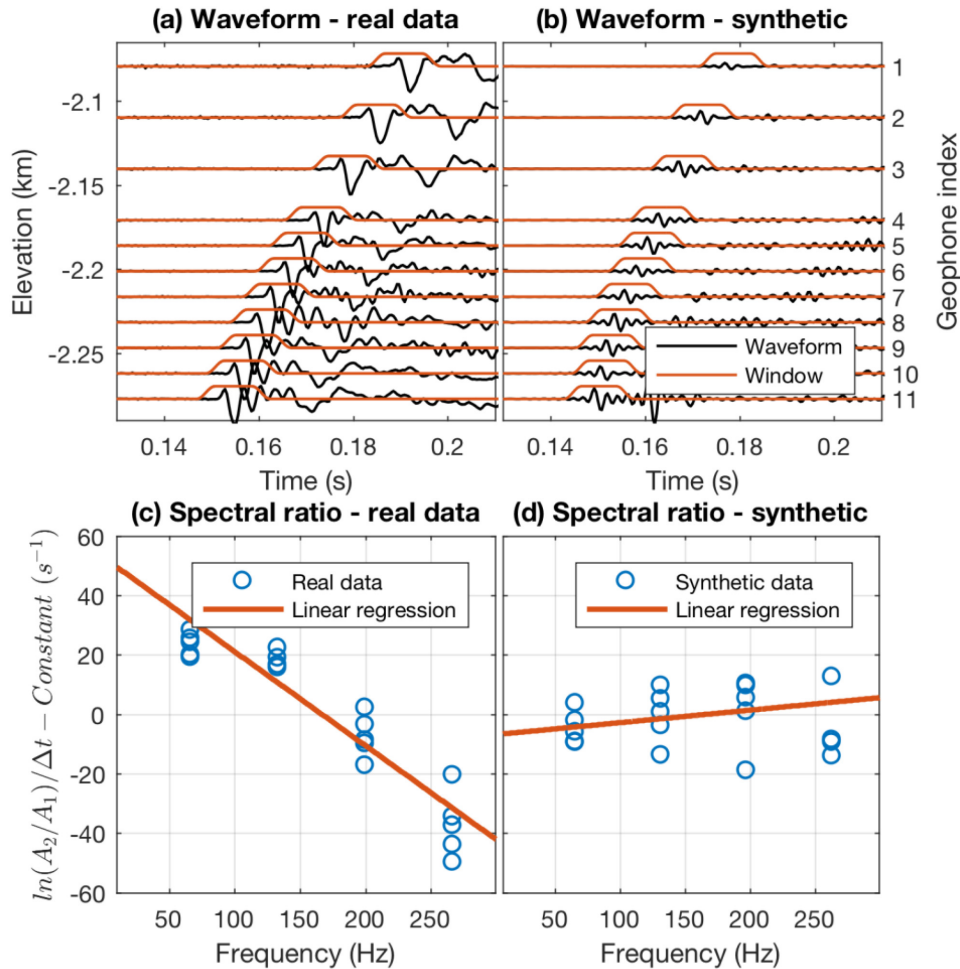


Figure 11. (a) Zoom-in view of the P -wave component of the waveform in Fig. 2. Comparing the waveforms from different geophones using the orange P -wave windows as reference, the dominant periods in the P -wave windows at the top traces are significantly longer than those at the bottom traces, which means the frequency contents of the P waves at the top traces are significantly lower than those at the bottom traces. This is an indication of severe attenuation. (b) Synthetic waveforms of the same perforation shot with (a). (c) Compiled spectral ratio of the waveforms in (a). (d) Compiled spectral ratio of the waveforms in (b). According to (b) and (d), there is no significant change in frequency content from geophones at the top to those at the bottom for the synthetic case.

5.3 Q_p and Q_s values from microseismic events

Since the estimation of Q values does not require information on source locations, we may also use waveforms from microseismic events to estimate Q values. Thanks to the shear-dominated nature of microseismic events (Fig. 8), the Q_s values can also be estimated with reasonable confidence. Here, we use the SH -wave portion of the waveform to estimate Q_s values. SV waves were not used due to low S/N. The histogram of Q_p and Q_s values obtained using microseismic event signals are shown in Fig. 14(b). The Q_p values from microseismic events are similar with those from perforation shots in Fig. 14(a). We also found that the Q_s values are significantly higher than the Q_p values within this region. This is not a result of statistical uncertainty since we also found similar results from a nearby well where there are more microseismic events with high S/N (not shown here for simplicity). One possible explanation to this smaller than 1 value of Q_p/Q_s is an indication of gas or condensate (Klimentos 1995), which is the case in this studied area.

5.4 Relating dispersion to attenuation

One possible explanation for the discrepancy between the MAP estimated model and the sonic log at the bottom layer is a result of velocity dispersion. Since we have observed severe attenuation within the studied area, causality requires a corresponding velocity dispersion (Toll 1956; Mavko *et al.* 2009). Thus, the sonic log may not be a good representation of the wave velocity at the microseismic frequency range. Here, we used a nearly constant Q model to explain the discrepancy between the MAP estimated velocity and the sonic log at the bottom layer (Liu *et al.* 1976; Mavko *et al.* 2009). According to the nearly constant Q model,

$$\frac{V(\omega)}{V(\omega_0)} = 1 + \frac{1}{\pi Q} \ln\left(\frac{\omega}{\omega_0}\right), \quad (11)$$

where $V(\omega)$ and $V(\omega_0)$ are velocities at two different frequencies ω and ω_0 and the Q value is assumed to be nearly constant within this seismic frequency band.

Assuming the picks of the arrival times represent a frequency of $\omega_0 = 200$ Hz, which is a typical resolvable frequency for microseismic survey, and the sonic log was acquired at a frequency of

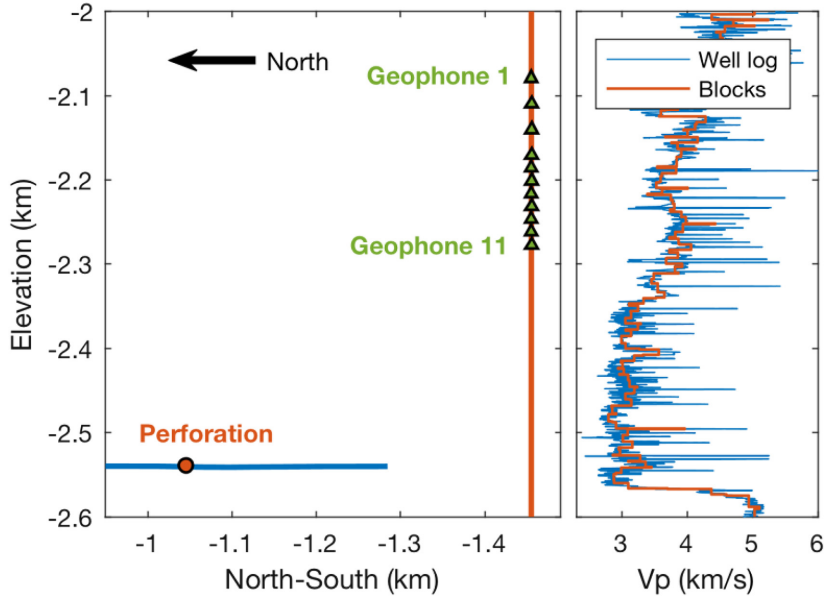


Figure 12. The model used to generate synthetic waveforms in Figs 11(b) and 13. We blocked the studied area into 154 layers as shown by the orange line based on sonic logs. The V_s values within each layer were calculated based on the assumption of $V_p/V_s = 1.73$. Densities were estimated with the Gardner's relation (Gardner *et al.* 1974). No intrinsic attenuation was assumed in the modelling to study the effect of stratigraphic scattering attenuation.

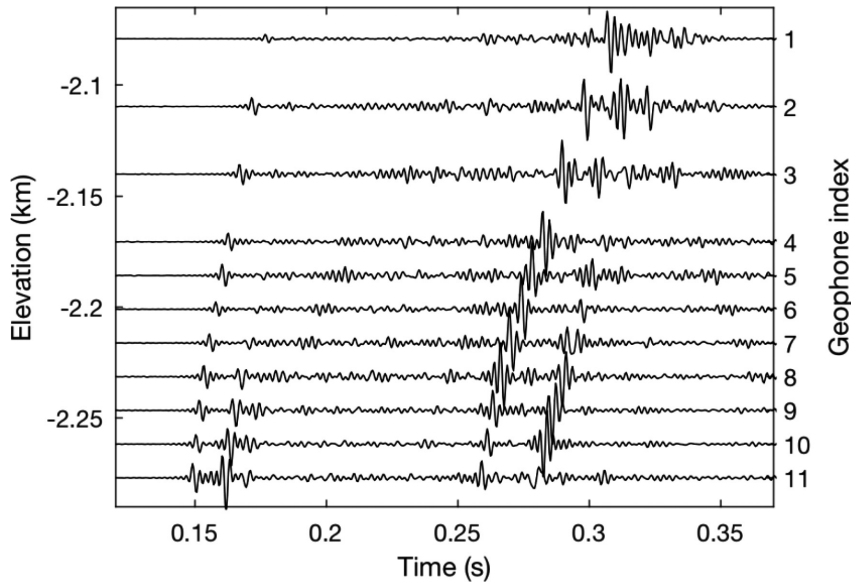


Figure 13. Synthetic seismogram from the earth model shown in Fig. 12. Significant coda wave can be observed due to the finely layered model used in the modelling. Both P - and S -wave reflections can be observed after the direct arrivals.

$\omega = 20$ kHz, which is a typical sonic log frequency, the left-hand side (LHS) of eq. (11) is

$$\text{LHS} = \frac{V_p(\omega)}{V_p(\omega_0)} = \frac{V_p(20 \text{ kHz})}{V_p(200 \text{ Hz})} \approx \frac{3.0 \text{ km s}^{-1}}{2.6 \text{ km s}^{-1}} \approx 1 + 0.15. \quad (12)$$

Using a Q_p value of 13 according to our estimation shown in Fig. 14, the right-hand side (RHS) of eq. (11) is

$$\text{RHS} = 1 + \frac{1}{\pi Q_p} \ln\left(\frac{\omega}{\omega_0}\right) \approx 1 + 0.11. \quad (13)$$

The LHS is approximately equal to the RHS of eq. (11) based on this analysis. This shows the attenuation at least partially explain

the discrepancy between the estimated velocity and the sonic log at the bottom layer.

Similar analysis can be made for S wave:

$$\text{LHS} = \frac{V_s(\omega)}{V_s(\omega_0)} = \frac{V_s(20 \text{ kHz})}{V_s(200 \text{ Hz})} \approx \frac{1.8 \text{ km s}^{-1}}{1.65 \text{ km s}^{-1}} \approx 1 + 0.09, \quad (14)$$

and

$$\text{RHS} = 1 + \frac{1}{\pi Q_s} \ln\left(\frac{\omega}{\omega_0}\right) \approx 1 + 0.05, \quad (15)$$

with a Q_s value of 30 according to Fig. 14(b). The LHS is on the same order of magnitude with the RHS. Admittedly, this is a rough estimation given the large uncertainty of the estimated velocity at the bottom layer (Fig. 9) and the homogenous and isotropic assumptions

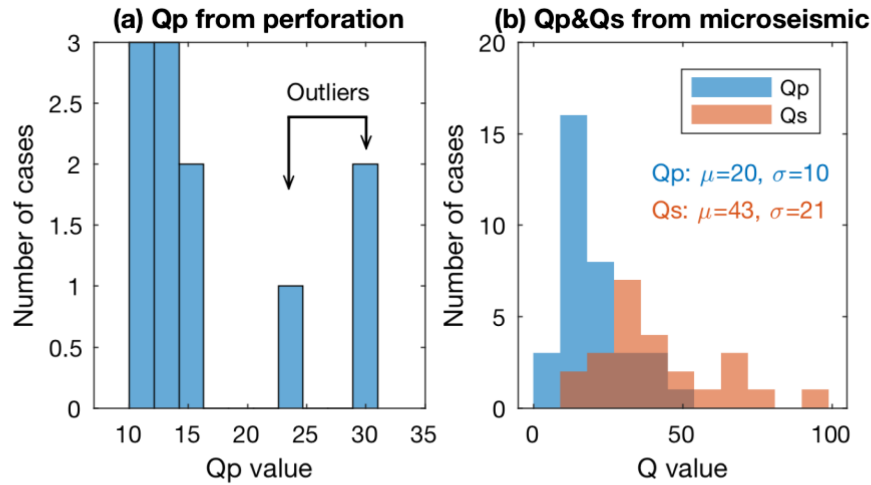


Figure 14. Histogram of Q values estimated with (a) perforation shots and (b) microseismic events. Q_s values cannot be estimated from perforation shots data due to the small portion of S -wave energy generated by explosive source. The Q_p values estimated using perforation shots lie mainly between 10 and 16. The three outliers between 23 and 30 will be discussed in Fig. 15. The Q_s values estimated with microseismic data are significantly larger than the estimated Q_p values.

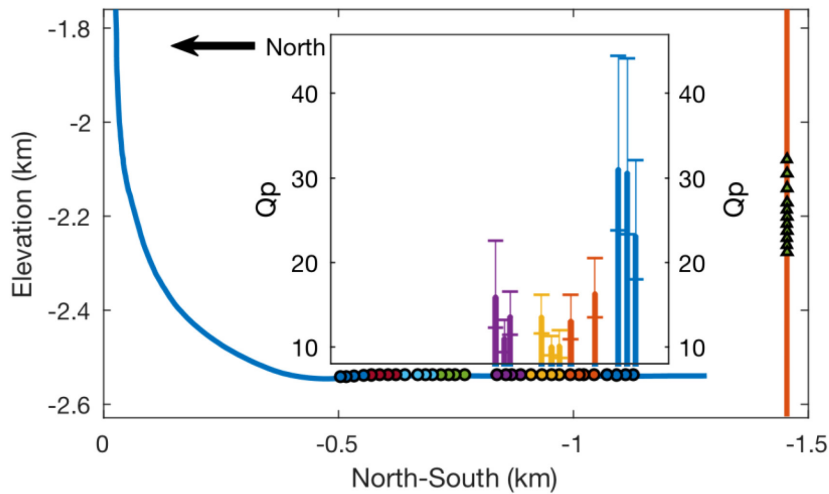


Figure 15. Estimated Q_p values using waveforms from perforation shots by stage and their 95 per cent confidence intervals. The Q_p values in Stage 1 (the three outliers in Fig. 14a) are significantly larger than those in the later stages. The decrease in Q_p values may result from hydraulic stimulation treatment after Stage 1 perforation.

of Q value. However, it indeed provides a plausible explanation to the discrepancy between the velocities from microseismic estimation and sonic log.

6 DISCUSSION

The vertical coverage of geophone arrays in a microseismic survey is usually limited, such as the case in this study. According to the RML uncertainty analysis, the velocity model estimation uncertainty significantly increases outside of the geophone depth range. A strategy to improve velocity estimation accuracy in the reservoir is to straddle the target area with a geophone array. However, this may lead to low S/N due to strong noise in this area. Distributed acoustic sensing, as an emerging technology (Karrenbach *et al.* 2017), could provide significantly improved coverage in the vertical direction. Thus, it has the potential to improve the accuracy of estimated earth model, and enable the characterization of depth variant attenuation using the method developed in this paper.

An assumption within this work is the homogenous Q model. This is due to the limited ray path coverage that can be used in this survey. Indeed, the effect of hydraulic stimulation should not be homogeneous along the whole seismic ray path. The Q values we obtained here should be considered as effective quality factors. However, it should still give an idea on how severe the attenuation induced by hydraulic stimulation might be. In addition, it provides a motivation to design a dedicated survey, such as crosswell, VSP or time-lapse seismic to monitor the hydraulic stimulation process. Efforts should be put to increase both source and receiver coverage to enable Q value tomography. Another difficulty brought by the limited ray path coverage lies in the estimation of stage-dependent velocity model. Ideally, the change of velocity and anisotropic parameters due to hydraulic stimulation can be observed by comparing the velocity model estimated using perforations in the first stimulation stage and that estimated using perforations in the later stimulation stages. However, the velocity model estimation using perforations only in the first stage is an underdetermined problem due to the limited ray path coverage, limited number of perforation shots and

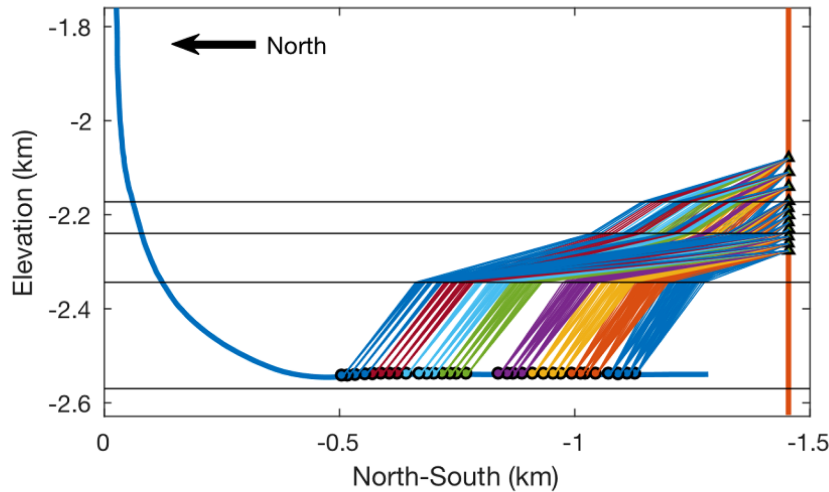


Figure 16. *P*-wave ray path coverage from perforation shots to geophones. Ray tracing was conducted with an isotropic model and is only for illustration purpose. Rays from Stages 2 to 8 perforation shots will cross stimulated zones of the previous stages; thus, affected by the previous stimulations.

the trade-offs among anisotropic earth model parameters. Simultaneous inversion for anisotropic parameters with microseismic data might be able to add information to stabilize the inversion and will be the next step of this work.

Both theoretical and laboratory rock physics studies need to be carried out to understand the change in Q values and the smaller-than-one Q_p/Q_s . The traditional practice of treating fractures as an effective medium (Kuster & Toksöz 1974; Cheng 1978; Hudson 1980; Hudson 1981; Cheng 1993) may be invalid for hydraulic fractures given the large scales of these fractures and short wavelength of seismic waves observed in downhole surveys. Possible effects that need to be considered include pore pressure change, gas/condensate saturation, squirt flow and scattering. Bergery *et al.* (2015) show that hydraulic stimulation may lead to severe *S*-wave energy attenuated with a data set from a nearby well. We were not able to extract temporally or spatially variant Q_s values from this data set with the presented method. As mentioned previously, a dedicated survey may help to improve attenuation characterization and the understanding of this effect. In addition, attenuation results in both amplitude loss and dispersion of seismic data (Zhu & Harris 2014). It may benefit to study attenuation from seismic wave amplitude point of view. However, the study of attenuation effect requires an understanding of the source radiation pattern, which is not well known for perforation shots.

7 CONCLUSIONS

With little requirement of sonic logs as the prior information, we were able to build an anisotropic earth model using only perforation shot data. RML estimation verifies the stability of the inversion and helps us to understand the uncertainties and trade-offs among velocity model parameters. The inverted vertically propagating V_p and V_s velocities match well with sonic log velocity data in areas that are unaffected by hydraulic stimulation. The magnitudes of inverted anisotropic parameters correlate well with clay contents from gamma-ray logs. Our work also suggests that the hydraulic stimulation process will cause significant increases to attenuation of seismic waves. Causality requires corresponding velocity dispersion associated with attenuation. Thus, traditional processing practice of using sonic logs, which are acquired at frequencies much higher than microseismic data frequency, may be questionable. It also shows

the possibility to monitor hydraulic stimulation with attenuation analysis.

ACKNOWLEDGEMENTS

We would like to thank Total S. A., Total Austral and its partners for granting permission to publish this paper. We thank ARMINES and Magnitude for providing access to the 3-D Anisotropic eikonal code. We also thank the two anonymous reviewers for their constructive comments and suggestions.

REFERENCES

- Amalokwu, K., Best, A.I., Sothcott, J., Chapman, M., Minshull, T. & Li, X.-Y., 2014. Water saturation effects on elastic wave attenuation in porous rocks with aligned fractures, *Geophys. J. Int.*, **197**, 943–947.
- Aster, R.C., Borchers, B. & Thurber, C.H., 2011. *Parameter Estimation and Inverse Problems*, Vol. **90**, Academic Press.
- Belayouni, N., Noble, M. & Gesret, A., 2016. 3D VTI wave attribute modelling tools for microseismic monitoring processing: traveltimes, amplitude and polarization, in *Sixth EAGE Workshop on Passive Seismic*, Muscat, Oman, doi:10.3997/2214-4609.201600015.
- Bergery, G., Grausem, M., Shuck, T. & Diller, D.E., 2015. Inferring the presence of fluid-filled fractures using *S*-wave attenuation on microseismic events, in *Proceedings of the 85th Annual International Meeting*, pp. 5037–5041, Society of Exploration Geophysicists.
- Bergery, G., Zhang, Z., Du, J., Diller, D., Shuck, T. & Fish, B., 2017. The plug drum effect, or why your microseismic events may not be where you think they are, in *Unconventional Resources Technology Conference*, pp. 2701–2710, Austin, Texas.
- Cheng, C.H., 1993. Crack models for a transversely isotropic medium, *J. geophys. Res.*, **98**, 675–684.
- Cheng, C.H.A., 1978. *Seismic Velocities in Porous Rocks: Direct and Inverse Problems*, Massachusetts Institute of Technology.
- Du, J., Warpinski, N. & Waltman, C., 2013. Anisotropic effects on polarization from highly deviated / horizontal wells in microseismic monitoring of hydraulic fractures, in *Proceedings of the 83rd Annual International Meeting*, pp. 2008–2012, Society of Exploration Geophysicists, pp. 2008–2012.
- Eisner, L., Gei, D., Hallo, M., Opršal, I. & Ali, M.Y., 2013. The peak frequency of direct waves for microseismic events, *Geophysics*, **78**, A45–A49.
- Garcia, M.N., Sorenson, F., Bonapace, J.C., Motta, F., Bajuk, C. & Stockman, H., 2013. Vaca muerta shale reservoir characterization and description:

- the starting point for development of a shale play with very good possibilities for a successful project, in *Unconventional Resources Technology Conference*, pp. 863–899, Denver, CO.
- Gardner, G.H.F., Gardner, L.W. & Gregory, A.R., 1974. Formation velocity and density—the diagnostic basics for stratigraphic traps, *Geophysics*, **39**, 770–780.
- Gesret, A., Desassis, N., Noble, M., Romary, T. & Maisons, C., 2015. Propagation of the velocity model uncertainties to the seismic event location, *Geophys. J. Int.*, **200**, 52–66.
- Grechka, V. & Heigl, W.M., 2017. *Microseismic Monitoring*, SEG.
- Grechka, V., Li, Z., Howell, B., Garcia, H. & Wooltorton, T., 2017. High-resolution microseismic imaging, *Leading Edge*, **36**, 822–828.
- Grechka, V., Singh, P. & Das, I., 2011. Estimation of effective anisotropy simultaneously with locations of microseismic events, *Geophysics*, **76**, WC143–WC155.
- Han, D.H., Nur, A. & Morgan, D., 1986. Effects of porosity and clay content on wave velocities in sandstones, *Geophysics*, **51**, 2093–2107.
- Herrmann, R.B., 2013. Computer programs in seismology: an evolving tool for instruction and research, *Seismol. Res. Lett.*, **84**, 1081–1088.
- Hudson, J., 1980. Overall properties of a cracked solid, in *Mathematical Proceedings of the Cambridge Philosophical Society*, pp. 371–384, Cambridge Univ Press.
- Hudson, J., 1981. Wave speeds and attenuation of elastic waves in material containing cracks, *Geophys. J. Int.*, **64**, 133–150.
- Karrenbach, M., Kahn, D., Cole, S., Ridge, A., Boone, K., Rich, J., Silver, K. & Langton, D., 2017. Hydraulic-fracturing-induced strain and microseismic using in situ distributed fiber-optic sensing, *Leading Edge*, **36**, 837–844.
- Klimentos, T., 1995. Attenuation of P- and S-waves as a method of distinguishing gas and condensate from oil and water, *Geophysics*, **60**, 447–458.
- Kuster, G.T. & Toksöz, M.N., 1974. Velocity and attenuation of seismic waves in two-phase media: Part I. Theoretical formulations, *Geophysics*, **39**, 587–606.
- Li, J., Zhang, H., Rodi, W.L. & Toksoz, M.N., 2013. Joint microseismic location and anisotropic tomography using differential arrival times and differential backazimuths, *Geophys. J. Int.*, **195**, 1917–1931.
- Li, Y., Wang, H., Fehler, M. & Fu, Y., 2017. Wavefield characterization of perforation shot signals in a shale gas reservoir, *Phys. Earth planet. Inter.*, **267**, 31–40.
- Liu, H.-P., Anderson, D.L. & Kanamori, H., 1976. Velocity dispersion due to anelasticity: implications for seismology and mantle composition, *Geophys. J. Int.*, **47**, 41–58.
- Mavko, G., Mukerji, T. & Dvorkin, J., 2009. *The Rock Physics Handbook: Tools for Seismic Analysis of Porous Media*, Cambridge Univ. Press.
- Maxwell, S., 2014. *Microseismic Imaging of Hydraulic Fracturing: Improved Engineering of Unconventional Shale Reservoirs*, SEG.
- Myers, S.C., Johannesson, G. & Hanley, W., 2007. A Bayesian hierarchical method for multiple-event seismic location, *Geophys. J. Int.*, **171**, 1049–1063.
- Nash, S.G., 2000. A survey of truncated-Newton methods, *J. Comput. Appl. Math.*, **124**, 45–59.
- Noble, M., Gesret, A. & Belayouni, N., 2014. Accurate 3-D finite difference computation of traveltimes in strongly heterogeneous media, *Geophys. J. Int.*, **199**, 1572–1585.
- Oliver, D.S., He, N. & Reynolds, A.C., 1996. Conditioning permeability fields to pressure data, in *ECMOR V-5th European Conference on the Mathematics of Oil Recovery*, doi:10.3997/2214-4609.201406884.
- Ou, L. & Prasad, M., 2016. Ultrasonic anisotropic P-wave attenuation of shales under elevated pressures, in *Proceedings of the 86th Annual International Meeting*, pp. 3261–3266, Society of Exploration Geophysicists, doi:10.1190/segam2016-13969715.1.
- Pan, W., Innanen, K.A. & Liao, W., 2017. Accelerating Hessian-free Gauss-Newton full-waveform inversion via l-BFGS preconditioned conjugate-gradient algorithm, *Geophysics*, **82**, R49–R64.
- Pei, D., Carmichael, J., Zhou, R. & Knappo, G., 2017. Enhanced microseismic anisotropic velocity optimization by check-shot and walkaway VSP, in *Proceedings of the 87th Annual International Meeting*, pp. 2867–2871, Society of Exploration Geophysicists.
- Pei, D., Quirein, J.A., Cornish, B.E., Quinn, D. & Warpinski, N.R., 2009. Velocity calibration for microseismic monitoring: a very fast simulated annealing (VFSA) approach for joint-objective optimization, *Geophysics*, **74**, WCB47–WCB55.
- Pratt, R.G., Shin, C. & Hick, G.J., 1998. Gauss–Newton and full Newton methods in frequency–space seismic waveform inversion, *Geophys. J. Int.*, **133**, 341–362.
- Quan, Y. & Harris, J.M., 1997. Seismic attenuation tomography using the frequency shift method, *Geophysics*, **62**, 895–905.
- Shapiro, S.A., 2015. *Fluid-Induced Seismicity*, Cambridge Univ. Press.
- Shen, Y., Biondi, B. & Clapp, R., 2018a. Q-model building using one-way wave-equation migration Q analysis — Part 1: theory and synthetic test, *Geophysics*, **83**, S93–S109.
- Shen, Y., Biondi, B. & Clapp, R., 2018b. Q-model building using one-way wave-equation migration Q analysis — Part 2: 3D field-data test, *Geophysics*, **83**, S111–S126.
- Tan, Y., Chai, C. & Engelder, T., 2014. Use of S-wave attenuation from perforation shots to map the growth of the stimulated reservoir volume in the Marcellus gas shale, *Leading Edge*, **33**, 1090–1096.
- Tarantola, A., 2005. *Inverse Problem Theory and Methods for Model Parameter Estimation*, Society for Industrial and Applied Mathematics (SIAM).
- Templeton, D.C., Johannesson, G. & Myers, S.C., 2014. An investigation of the microseismicity at the newberry EGS Site, Stanford University, CA, in *Proceedings of Thirty-Ninth Workshop on Geothermal Reservoir Engineering*, Stanford University, California.
- Thomsen, L., 1986. Weak elastic anisotropy, *Geophysics*, **51**, 1954–1966.
- Toll, J.S., 1956. Causality and the dispersion relation: logical foundations, *Phys. Rev.*, **104**, 1760–1770.
- Tonn, R., 1991. The determination of the seismic quality factor Q from VSP data: a comparison of different computational methods, *Geophys. Prospect.*, **39**, 1–27.
- Vera Rodriguez, I. & Stanchits, S., 2017. Spatial and temporal variation of seismic attenuation during hydraulic fracturing of a sandstone block subjected to triaxial stress, *J. geophys. Res.*, **122**(11), 9012–9030.
- Vernik, L., 2016. *Seismic Petrophysics in Quantitative Interpretation*, Society of Exploration Geophysicists.
- Vernik, L. & Nur, A., 1992. Ultrasonic velocity and anisotropy of hydrocarbon source rocks, *Geophysics*, **57**, 727–735.
- Wandycz, P., Świąch, E., Eisner, L., Maćkowski, T. & Pasternacki, A., 2017. Estimation of the quality factor using peak frequency method in polish shale gas deposits, in *79th EAGE Conference and Exhibition*, Paris, France, doi:10.3997/2214-4609.201701487.
- Wcisło, M. & Eisner, L., 2016. Attenuation from microseismic datasets by the peak frequency method benchmarked with the spectral ratio method, *Stud. Geophys. Geod.*, **60**, 547–564.
- Wcisło, M. & Eisner, L., 2017. Automated determination of attenuation from microseismic events, in *79th EAGE Conference and Exhibition*, Paris, France, doi:10.3997/2214-4609.201701334.
- Willis, M., Tutuncu, A.N. & Padin, A., 2014. Integration of core data with well logs for geomechanical property determination and monitoring in the argentinean vaca muerta shale formation, in *Unconventional Resources Technology Conference*, pp. 1715–1729, Denver, CO, doi:10.15530/urtec-2014-1922481.
- Yuan, D. & Li, A., 2017. Joint inversion for effective anisotropic velocity model and event locations using S-wave splitting measurements from downhole microseismic data, *Geophysics*, **82**, C133–C143.
- Zhang, Z., Du, J. & Gao, F., 2017a. Simultaneous inversion for microseismic event location and velocity model in vaca muerta formation, in *Unconventional Resources Technology Conference*, 26–45, Unconventional Resources Technology Conference, Austin, Texas.
- Zhang, Z., Du, J. & Gao, F., 2018. Simultaneous inversion for microseismic event location and velocity model in Vaca Muerta Formation, *Geophysics*, **83**, KS23–KS34.
- Zhang, Z., Jafarpour, B. & Li, L., 2014. Inference of permeability heterogeneity from joint inversion of transient flow and temperature data, *Water Resour. Res.*, **50**, 4710–4725.

- Zhang, Z., Rector, J.W. & Nava, M.J., 2017b. Simultaneous inversion of multiple microseismic data for event locations and velocity model with Bayesian inference, *Geophysics*, **82**, KS27–KS39.
- Zhu, H., Li, S., Fomel, S., Stadler, G. & Ghattas, O., 2016. A Bayesian approach to estimate uncertainty for full-waveform inversion using a priori information from depth migration, *Geophysics*, **81**, R307–R323.
- Zhu, T., Ajo-Franklin, J.B. & Daley, T.M., 2017. Spatiotemporal changes of seismic attenuation caused by injected CO₂ at the Frio-II pilot site, Dayton, TX, USA, *J. geophys. Res.*, **122**, 7156–7171.
- Zhu, T. & Harris, J.M., 2014. Modeling acoustic wave propagation in heterogeneous attenuating media using decoupled fractional Laplacians, *Geophysics*, **79**, T105–T116.